Applied Catalysis B: Environmental 321 (2023) 121970

Contents lists available at ScienceDirect

Applied Catalysis B: Environmental

journal homepage: www.elsevier.com/locate/apcatb

Hydroxyl radical streaming from molecular oxygen activation by β-$FeC_2O_4{\cdot}2H_2O$ for efficiently degrading Microcystin-LR

Qian Fu [a], Yi Mu [a,*], Lixia Yang [a], Yi Mei [a], Meifeng Wu [a], Jian-Ping Zou [a], Dionysios D. Dionysiou [b], Shenglian Luo [a,*]

[a] Key Laboratory of Jiangxi Province for Persistent Pollutants Control and Resources Recycle, Nanchang Hangkong University, Nanchang 330063, People's Republic of China

[b] Environmental Engineering and Science Program, Department of Chemical and Environmental Engineering, University of Cincinnati, Cincinnati, OH 45221, USA

ARTICLE INFO

Keywords:
MC-LR
Molecular oxygen activation
β-$FeC_2O_4{\cdot}2H_2O$
Hydroxyl radical
Electron utilization efficiency

ABSTRACT

In this study, β-$FeC_2O_4{\cdot}2H_2O$ was employed to activate molecular oxygen for the generation of abundant hydroxyl radicals (•OH) for efficient degradation of toxic Microcystin-LR (MC-LR) at ambient conditions. Specifically, dioxygen is selectively reduced to H_2O_2 through a two-electron transfer pathway on the (0 2 2) facet of β-$FeC_2O_4{\cdot}2H_2O$ crystals, and then H_2O_2 reacts with Fe(II) to form •OH. The electron utilization efficiency of β-$FeC_2O_4{\cdot}2H_2O$ toward •OH is high up to 87.7%, ensuring the formation of a sustainable •OH stream. In addition, the Fe^{3+} generated from β-$FeC_2O_4{\cdot}2H_2O$ oxygenation coordinates with oxalate to form soluble $[Fe^{3+}\text{-}(C_2O_4^{2-})_2]^-$ complex, avoiding the formation of passivated Fe(III) oxide/hydroxide shell on β-$FeC_2O_4{\cdot}2H_2O$ and enabling the long durability of β-$FeC_2O_4{\cdot}2H_2O$. When MC-LR is oxidized, the •OH primarily attacks the conjugated dienes (the essential group for the hepatotoxicity) in the Adda side chain of MC-LR. The toxicity assessment by PP2A test shows that the oxidation products are not hepatotoxins. As β-$FeC_2O_4{\cdot}2H_2O$ governing water treatment is easily manipulated, cost-effective, highly effectual, environmentally benign as well, it is promising to eliminate MC-LR contamination in natural waters and can be applied in large scale.

1. Introduction

Recently, the frequent break-out of cyanobacterial harmful algal blooms (cyano-HABs) caused by nutrient over-enrichment and global warming have raised critical concerns about the safety of drinking water resources as the microcystins (MCs), the toxic metabolites produced by cyano-HABs, present extreme threats (carcinogenesis, damage of liver, kidney, and heart) to health of human beings [1–3]. Among the numerous MCs, microcystin-leucine arginine (MC-LR) is one of the most toxic (Rat LD_{50} is 50 μg/kg) and abundant in natural waters [4]. The World Health Organization (W. H. O) recommends that the value of MC-LR in drinking water should be no more than 1 μg/L based on its toxicity toward human beings [5].

To date, various technologies, including Fenton reaction [6], electrochemical oxidation [7], and photo-oxidation (including photolysis and photocatalysis) [8–11], have been proposed to remove MC-LR. However, these strategies suffer from complex manipulation, possible secondary pollution or high operating cost. Molecular oxygen (O_2) is the greenest and abundant oxidant in natural waters [12]. But direct oxidation of MC-LR by O_2 under ambient condition is hardly achieved because of the spin-forbidden nature of O_2 [13]. Lately, a series of iron-based materials (such as granular or nanoscale zero-valent iron (ZVI) [14–16], ferrous sulfides [17,18], bimetallic materials [19,20]) were used to activate O_2 to produce hydroxyl radical (•OH) (Eq. 1 - 4) which could efficiently destroy various persistent organic pollutants including MC-LR. Nevertheless, the electron utilization efficiency of the iron-based materials toward •OH yield is typically less than 10% [21], which may dramatically restrict their practical application.

$$O_2 + Fe(s)^0 + 2H^+ = H_2O_2 + Fe^{2+} \quad (1)$$

$$O_2 + Fe^{2+} = \cdot O_2^- + Fe^{3+} \quad (2)$$

$$\cdot O_2^- + Fe^{2+} + 2H^+ = Fe^{3+} + H_2O_2 \quad (3)$$

$$H_2O_2 + Fe^{2+} = \cdot OH + Fe^{3+} + OH^- \quad (4)$$

* Corresponding authors.
E-mail addresses: my812852435@163.com (Y. Mu), sllou@hnu.edu.cn (S. Luo).

https://doi.org/10.1016/j.apcatb.2022.121970
Received 12 July 2022; Received in revised form 2 September 2022; Accepted 5 September 2022
Available online 8 September 2022

So far, a number of organic/inorganic ligands, such as ethylenediamine tetraacetate (EDTA), citrate (CIT), tetrapolyphosphate (TPP), and polyoxometalate (POM), were introduced to enhance •OH generation during molecular oxygen activation with iron-based materials [22–27]. The primary role of the ligands is iron-chelation, which increases the solubility of Fe(III) and prevents formation of passivated Fe(III) oxide/hydroxide shell on the surface of iron-based materials. However, organic ligands can consume •OH, lowering the degradation efficiency of pollutants, and their emission to the environment can also cause severe secondary pollution [28]. What's more, the electron utilization efficiency toward •OH generation is still far from satisfactory. This is because a too strong interaction is formed between the reaction site and O_2, which easily dissociates the O–O bond of O_2 and facilitates direct conversion of O_2 to H_2O (Eq 5) [29]. Obviously, this problem is difficult to be solved by the above-mentioned ligand-adding approaches. Therefore, searching for an iron-based material with proper binding strength between O_2 and reaction site for efficient •OH generation is of great significance in the remediation of MC-LR pollution.

$$O_2 + 2Fe(s)^0 + 4H^+ = 2Fe^{2+} + 2H_2O \quad (5)$$

Recent studies have found that the iron atom adjacent to several oxygen functional groups (-COOH and C-O-C) is the active site for creating H_2O_2 from electron-reduction of O_2 through a two-electron transfer pathway [30]. This is mainly due to the unique electronic properties of the single Fe atom as well as its adjacent coordination environment (Fe-O-C), which endows proper binding strength between the Fe atom with O_2 for efficient H_2O_2 generation [31,32]. Ferrous oxalate dihydrate ($FeC_2O_4{\cdot}2H_2O$), so-called humboldtine in the field of mineralogy, is one of the simplest coordinated polymers and widely exists in brown coal and soil [33]. It has an extended one-dimensional network and each Fe(II) atom coordinates to oxalate unit via Fe-O-C bond. Analogously, the typical Fe-(O_2)C-C(O_2) structure in $FeC_2O_4{\cdot}2H_2O$ may endow it with proper binding strength with O_2. Besides, it has excellent performance to provide abundant electrons [34,35], thus may achieve continuous and efficient H_2O_2 production through oxygen reduction reaction (ORR). Furthermore, $FeC_2O_4{\cdot}2H_2O$ with abundant Fe^{2+} in the layered structure could directly capture and activate H_2O_2 to produce •OH. Therefore, we hypothesized that $FeC_2O_4{\cdot}2H_2O$ featuring the synergistic effects of H_2O_2 generation and activation would be an attractive iron-based candidate for the generation of •OH and degradation of MC-LR.

Herein, the MC-LR degradation efficiency in the β-$FeC_2O_4{\cdot}2H_2O/O_2$ system was investigated in detail. Meanwhile, the reactive oxygen species (ROS, i.e., H_2O_2 and •OH) yields and the electron utilization efficiency of β-$FeC_2O_4{\cdot}2H_2O$ toward •OH generation were determined. Subsequently, the mechanism of molecular oxygen activation by β-$FeC_2O_4{\cdot}2H_2O$ for •OH generation was systematically studied with help of rotating ring disk electrochemical analysis, various advanced characterization techniques, and theoretical calculations. In particular, the association between surface structure and molecular O_2 activation of β-$FeC_2O_4{\cdot}2H_2O$ was revealed. By identifying the final products from MC-LR degradation, the pathway illustrating the degradation details concerning MC-LR was proposed. Moreover, the PP2A activity test demonstrated that the hepatotoxicity of MC-LR degradation products was completely eliminated, leaving no acute toxicity effects. This work proposes a new strategy to activate O_2 for the efficient •OH generation along with a profound insight about the involved mechanism.

2. Experiment section

2.1. Reagents

Ferrous sulfate heptahydrate (≥ 99.0 %), oxalic acid dihydrate (≥ 99.0 %), sodium hydroxide (≥ 96.0 %), sulfuric acid (98.0 %), methanol (≥ 99.5 %) and *tert*-butyl alcohol (≥ 99.5 %) were bought from National Medicines Corporation Ltd., China. Superoxide dismutase (SOD; ≥ 1400 U mg^{-1} protein) and catalase (CAT; ≥ 100 U mg^{-1} protein) were obtained from Shanghai Yuanye Bio-Technology Co. Ltd. Microcystin-leucine arginine (MC-LR) was bought from Agent Technology Co., Ltd. The detailed procedure for synthesis of β-$FeC_2O_4{\cdot}2H_2O$ is provided in Text S1 in SI.

2.2. Degradation experiments

In the typical MC-LR degradation experiment, β-$FeC_2O_4{\cdot}2H_2O$ (0.018 g) was added into the conical glass flask containing 100 mL of MC-LR solution (1.0 mg/L). The conical flask was then transferred into a shaker, and the rotate speed was set at 200 rpm. The temperature was kept at 25 °C during the reaction. At regular intervals, the degradation solutions were taken out with a syringe and filtered through a nylon syringe filter (0.22 μm) to separate β-$FeC_2O_4{\cdot}2H_2O$. Subsequently, methanol (0.5 mL) was added into the sampled solution (1.5 mL) to prevent further degradation of MC-LR. The O_2-free control experiment was performed in Ar-purged solution. The reacted β-$FeC_2O_4{\cdot}2H_2O$ was obtained through centrifugal separation and dried at 60 °C under vacuum condition for subsequent characterization.

2.3. Analytical methods

A high-performance liquid chromatography was used to determine the concentrations of MC-LR and the oxidation products of benzoic acid. The concentration of total iron dissolved in aqueous solution was measured by a flame atomic absorption spectrometer (FAAS) (Analytik, Jena, Germany). The concentration of Fe(II) was determined by 1,10-phenanthroline method. The concentration of Fe(III) was calculated from the difference between the total dissolved iron and Fe(II). A high-performance liquid chromatography with electro-spray ionization high-resolution mass spectrometry was applied to identify the products of β-$FeC_2O_4{\cdot}2H_2O$ oxygenation in the solutions. The detailed information about the analytical methods was provided in Supporting Information (Text S2 in SI). The concentration of hydrogen peroxide (H_2O_2) was determined spectrophotometrically using the $Ce(SO_4)_2$ method [30]. The hepatotoxicities of MC-LR and its transformation products in the reaction solution were evaluated by the PP2A activity assay [36], and the detailed information is presented in Text S3 in SI.

2.4. Characterizations

The electron transfer numbers (n) of ORR on the surface of β-$FeC_2O_4{\cdot}2H_2O$ were calculated by the rotating disc electrode (RDE) experiment [37]. The detailed information about RDE experiment is presented in Text S4 in SI. The crystal phase structures of the as-synthesized samples were characterized by X-ray powder diffraction (Bruker D8 ADVANCE) using graphite monochromatized Cu Kα (λ = 1.5406 Å) radiation, and the range of 2θ = 10–60° was scanned at a rate of 2°/min. Scanning electron microscope (FEI, Holland) and transmission electron microscope (Tecnai F20, FEI, USA) were used to observe the morphology of the samples. The surface chemical characteristic of the sample was identified by X-ray photoelectron spectroscopy (PHI 5700 ESCA System, USA).

2.5. Theoretical calculations

Density functional theory (DFT) calculations were carried out to simulate the adsorption behavior of O_2 and oxygen reduction reaction on the surface of β-$FeC_2O_4{\cdot}2H_2O$ with Materials Studio-DMol^3 code. The detailed information about calculation procedure is provided in Text S5 in SI.

3. Results and discussion

3.1. Degradation of MC-LR by β-FeC_2O_4·$2H_2O$

Degradation of MC-LR by β-FeC_2O_4·$2H_2O$ was conducted under aerobic condition at 25 °C. As shown in Fig. 1a, almost all MC-LR is degraded within 12 h at initial pH 6.50. The degradation curve obeys the pseudo-first-order kinetic equation and the rate constant is determined to be 0.2689 h^{-1} (Fig. S1). For comparison, MC-LR degradation by sole Fe^{2+} and oxalic acid at initial pH 6.50 is very slow. Only 43.6% of MC-LR is removed in the $Fe^{2+}/C_2O_4^{2-}/O_2$ system within 12 h ($k = 0.0474\ h^{-1}$). Besides, negligible MC-LR is removed in the β-FeC_2O_4·$2H_2O$/Ar system, verifying the importance of simultaneous presence of β-FeC_2O_4·$2H_2O$ and O_2 in the degradation of MC-LR. In addition, the MC-LR degradation performance of β-FeC_2O_4·$2H_2O$ was compared with other iron-based materials (such as nZVI, FeS, FeS_2, and $FeCO_3$) because all them had potential for activating molecular O_2 to generate •OH [17]. As exhibited in Fig. S2, oxidative degradation of MC-LR by β-FeC_2O_4·$2H_2O$ is much more efficient than those of iron-based materials at identical conditions. These results indicate that β-FeC_2O_4·$2H_2O$ can efficiently activate O_2 to form reactive oxygen species for the removal of MC-LR.

3.2. Identification and quantification of ROS

Spin-trapping EPR technique was employed to identify the short-lived reactive species (such as $•O_2^-$, •OH) generated in the β-FeC_2O_4·$2H_2O/O_2$ system. DMPO was used as a spin-trapping agent. As shown in Fig. 1b, the typical pattern of DMPO-•OH adduct is observed in the β-FeC_2O_4·$2H_2O/O_2$ system after 2 h of reaction. But such a signal is not detected in the β-FeC_2O_4·$2H_2O$/Ar system. This result confirms that β-FeC_2O_4·$2H_2O$ can activate molecular oxygen to form •OH. To further determine the individual contribution of reactive species in degradation of MC-LR, a series of scavenging experiments were performed in the β-FeC_2O_4·$2H_2O/O_2$ system by adding different scavengers (SOD for $•O_2^-$, TBA for •OH, and catalase for H_2O_2, respectively) (Fig. S3). As exhibited in Fig. 1c, the degradation rate constant (k) of MC-LR decreased from 0.2689 h^{-1} without scavengers to 0.2508, 0.0175, and 0.0025 h^{-1} in the presence of SOD, catalase, and TBA, respectively. We calculated the inhibitory efficiency (η) of the different scavengers with Eq. 6.

$$\eta\% = ((k - k_s)/k) \times 100\% \quad (6)$$

MC-LR degradation rate constant is merely declined by 2.7% in the presence of SOD, ruling out the contribution of $•O_2^-$ on MC-LR degradation in the β-FeC_2O_4·$2H_2O/O_2$ system. Meanwhile, TBA almost completely suppresses the degradation of MC-LR, further confirming that •OH is the major reactive species and responsible for MC-LR

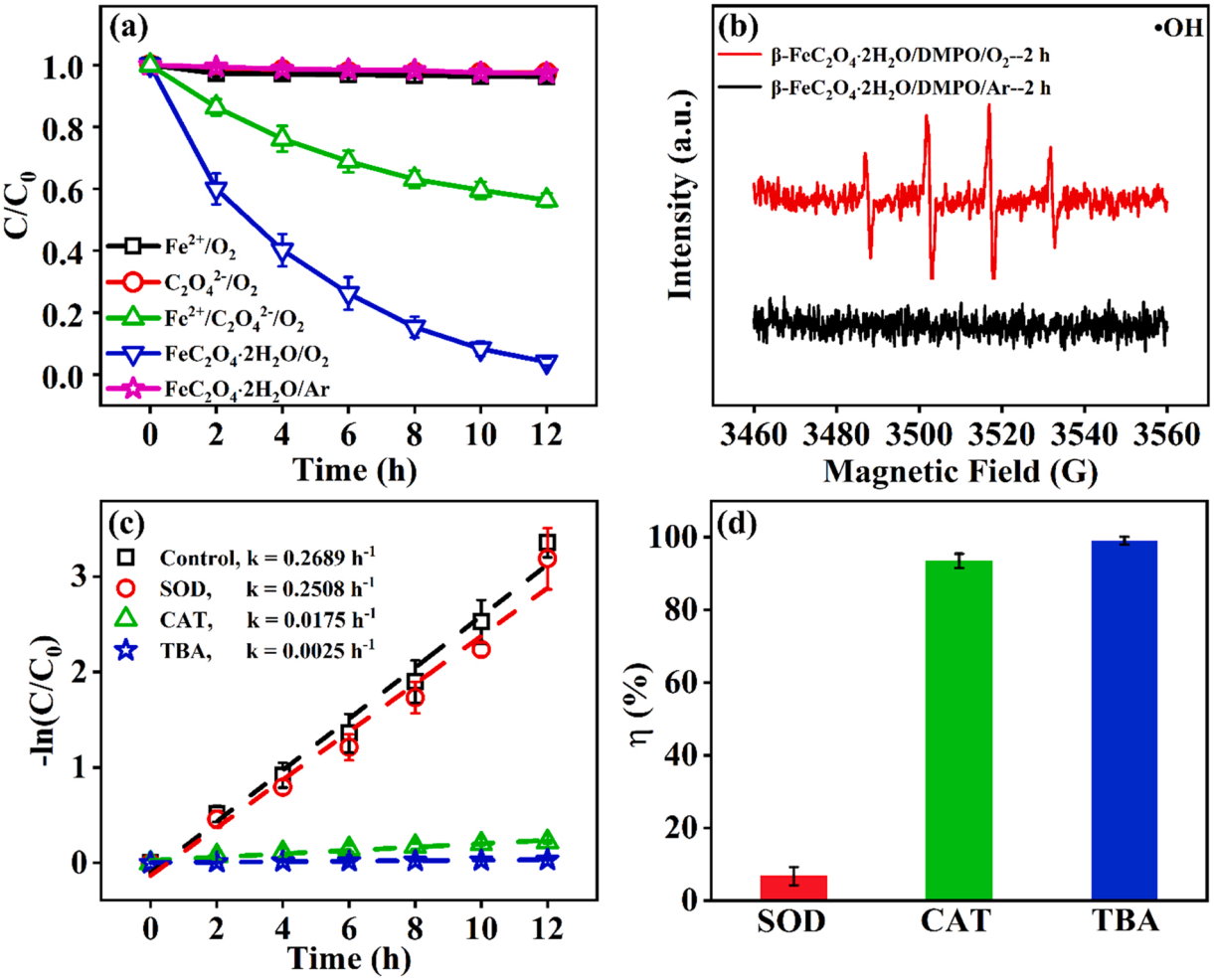

Fig. 1. (a) Time profiles of the aerobic MC-LR degradation in different systems. The initial concentration of MC-LR was 1.0 mg/L. The initial concentrations of Fe^{2+}, oxalic acid, and β-FeC_2O_4·$2H_2O$ were 1.0 mmol/L. The initial pH values were 6.50. (b) EPR spectra of DMPO spin-trapping •OH radical obtained from β-FeC_2O_4·$2H_2O/O_2$ (red line) and β-FeC_2O_4·$2H_2O$/Ar (black line) systems. (c) Plots of ln(C_0/C) versus time for MC-LR degradation in the β-FeC_2O_4·$2H_2O/O_2$ systems with addition of different scavengers (TBA for •OH, CAT for H_2O_2, SOD for $•O_2^-$). The initial concentrations of the TBA, CAT and SOD were 200 mmol/L, 100 mg/L, and 100 mg/L, respectively. (d) The inhibitory efficiency (η) of different scavengers during MC-LR degradation in the β-FeC_2O_4·$2H_2O/O_2$ system.

degradation. As the degradation rate is decreased by 93.5% with catalase, it turns out that H_2O_2 is the dominant intermediate for the formation of •OH.

To further verify above assumption, we determined the amount of ROS (i.e., H_2O_2 and •OH) generated in the •OH)$_2O_4$·$2H_2O/O_2$ system. As Fig. S4 reveals, the concentration of H_2O_2 is increased as a function of reaction time and approaches a constant value (167.93 μmol/L) within 12 h while it is negligible under anaerobic condition, confirming that H_2O_2 is mainly derived from O_2 reduction by β-FeC_2O_4·$2H_2O$. Thereafter, we quantitatively measured the amount of •OH generated via molecular oxygen activation by β-FeC_2O_4·$2H_2O$ and estimated the electron utilization efficiency toward •OH. The cumulative concentration of •OH was quantified using hydroxylation of benzoic acid as a probe reaction [38]. The initial concentration of benzoic acid was set at 10.0 mmol/L to make sure all •OH react with benzoic acid. Four organic acids are produced from this reaction (Fig. 2a), including salicylic acid (2-HBA, retention time: 23.43 min, λ_{max}: 300 nm), 3-hydroxybenzoic acid (3-HBA, retention time: 10.69 min, λ_{max}: 300 nm), 4-hydroxybenzoic acid (4-HBA, retention time: 8.06 min, λ_{max}: 276 nm), and 2,5-dihydroxybenzoic acid (2,5-DHBA, retention time: 9.55 min, λ_{max}: 330 nm). The concentrations of these hydroxybenzoate products are increased gradually with reaction time and accumulated to 35.77 μmol/L (2-HBA), 30.05 μmol/L (3-HBA), 23.92 μmol/L (4-HBA), and 101.27 μmol/L (2, 5-DHBA) within 192 h (Fig. 2b). The cumulative concentration of •OH produced from molecular oxygen activation with β-FeC_2O_4·$2H_2O$ is determined to be 292.28 μmol/L by Eq. 7. Meanwhile, the concentration of Fe(III) released into aqueous solution is increased as function of reaction time and gradually approaches the steady value of 1.0 mmo/L after 192 h of reaction (Fig. S5), suggesting that all of Fe(II) species of β-FeC_2O_4·$2H_2O$ are involved in the molecular oxygen activation process. In addition, it is found that negligible hydroxybenzoate products is generated in the $Fe^{3+}/C_2O_4^{2-}/O_2$ system (data not shown), indicating O_2 can not be activated by Fe^{3+} and $C_2O_4^{2-}$ to produce •OH. It is believed that all the electron involved in •OH generation is derived from Fe(II) species of β-FeC_2O_4·$2H_2O$. In theory, three Fe(II) in β-FeC_2O_4·$2H_2O$ polymer are consumed to produce one •OH (Eq. 8- Eq. 9). The electron utilization efficiency (η_e) of β-FeC_2O_4·$2H_2O$ toward •OH generation is defined by Eq. 10, and η_e is calculated to be 87.7%. For comparison, the electron utilization efficiency (η_e) of nZVI, FeS, FeS_2, and $FeCO_3$ toward •OH generation is determined to be 0.11 %, 9.22 %, 0.47 % and 3.55 %, respectively (Figs. S6-S8, the detailed calculation procedures were provided in Text S6 in Supporting Information). Obviously, β-FeC_2O_4·$2H_2O$ presents exceptional performance towards •OH generation in terms of high electron utilization efficiency. We therefore conclude that O_2 can be activated by β-FeC_2O_4·$2H_2O$ to produce plenty of ROS for the efficient degradation of MC-LR under ambient condition.

According to previous study [38], surface-bound •OH reacting with benzoic acid may lead to extensive generation of 2,5-DHBA. As shown in Fig. 2b, the major oxidation product of benzoic acid is 2,5-DHBA and its ratio with respect to the total hydroxylated products is 53.0%. This result indicates that surface-bound •OH is the dominant reactive species in the β-FeC_2O_4·$2H_2O/O_2$ system. Thereby, it is proposed that molecular oxygen action and subsequent •OH generation mainly occur at surface of β-FeC_2O_4·$2H_2O$ rather than in aqueous solution.

$$[\cdot OH] = [2-HBA] + [3-HBA] + [4-HBA] + 2 \times [2,5-DHBA] \quad (7)$$

$$2\beta - FeC_2O_4 \cdot 2H_2O + O_2 = 2Fe^{3+} + H_2O_2 + 2H_2O + 2OH^- + 2C_2O_4^{2-} \quad (8)$$

$$\beta - FeC_2O_4 \cdot 2H_2O + H_2O_2 = Fe^{3+} + \cdot OH + 2H_2O + OH^- + C_2O_4^{2-} \quad (9)$$

$$\eta_e(\%) = 3 \times [\cdot OH]/1\ \text{mmol/L} \times 100\% \quad (10)$$

3.3. The oxygen reduction pathway on β-FeC_2O_4·$2H_2O$ for ROS generation

According to previous studies, H_2O_2 can be produced through either a two-electron transfer pathway (Eq. 1) or a sequential single-electron transfer pathway (Eq. 2 - 3) [39]. The scavenging experiment reveals that SOD merely poses a drop of 2.7% regarding MC-LR degradation, indicating that the single-electron transfer is not the dominant pathway of O_2 reduction for H_2O_2 generation in the β-FeC_2O_4·$2H_2O/O_2$ system. As a result, it is probable that the generation of H_2O_2 follows a direct two-electron transfer ($O_2 \rightarrow H_2O_2$) pathway [40,41]. To verify the above assumption, a rotating disc electrode experiment was conducted to calculate the electron transfer number of O_2 reduction reaction on β-FeC_2O_4·$2\ H_2O$ surface [42]. The linear sweep voltammetry (LSV) of rotating β-FeC_2O_4·$2\ H_2O$ film glassy carbon disc electrode in KOH solution (0.1 mol/L) was obtained at rotating rates of 400, 625, 900, 1225, and 1600 rpm, respectively (Fig. 3a). The plateau currents were determined at a potential of 0.45 V. Koutecky-Levich equation was then employed to estimate the electron transfer number of ORR at plateau currents. According to Eq. 11, current density (J) is consisted of a kinetic

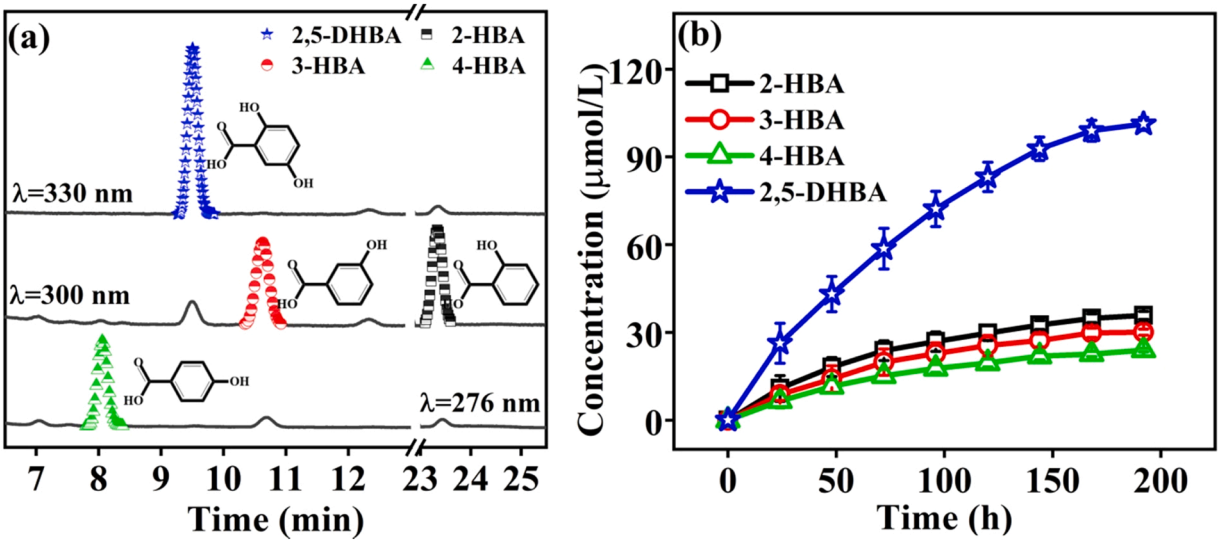

Fig. 2. (a) The HPLC chromatograms of oxidation products of benzoic acid sampled at 192 h in the β-FeC_2O_4·$2H_2O/O_2$ system. (b) Temporal concentrations of degradation intermediates during benzoic acid degradation as a function of time in the β-FeC_2O_4·$2H_2O/O_2$ system. The initial concentrations of β-FeC_2O_4·$2H_2O$ and benzoic acid were 1.0 mmol/L and 10.0 mmol/L, respectively. The initial pH value was 6.50.

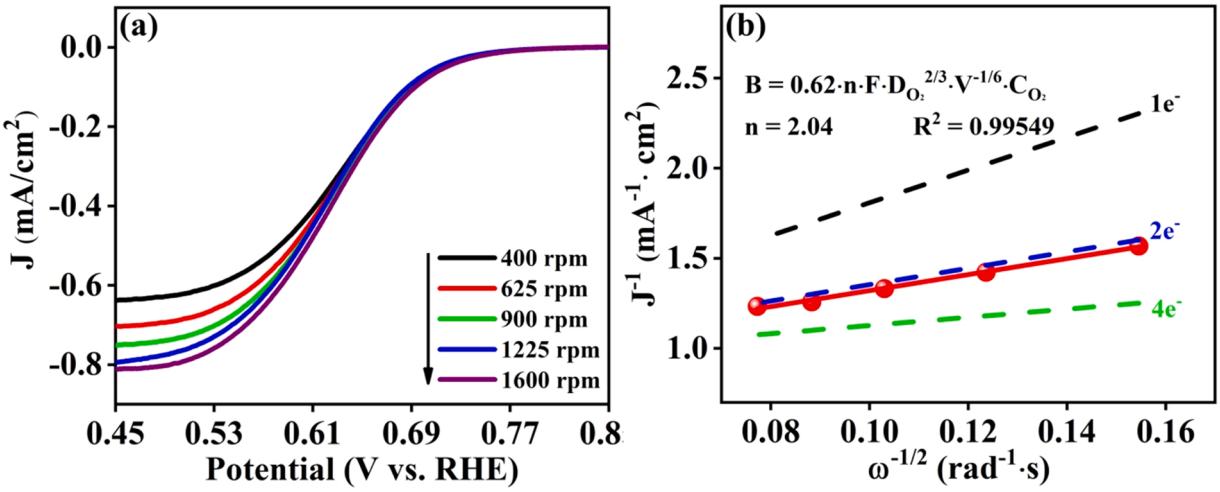

Fig. 3. (a) Linear scanning voltammetry (LSV) of rotating β-FeC_2O_4·$2H_2O$ film disc electrode in O_2-saturated 0.1 mol/L KOH solutions (pH 13), at rotating rates of 400, 625, 900, 1225, and 1600 rpm. (b) Koutecky-Levich plots of β-FeC_2O_4·$2H_2O$ film at plateau currents. The dashed lines show the standard slopes for n = 1, 2, and 4.

part (J_{kin}) and a diffusion part (J_{diff}).

$$\frac{1}{J}=\frac{1}{J_{Kin}}+\frac{1}{J_{diff}}=\frac{1}{J_{Kin}}+\frac{1}{B\sqrt{\omega}} \tag{11}$$

in which B factor is determined by

$$B=0.62\bullet n\bullet F\bullet V^{-1/6}\bullet C_{O_2}\bullet D_{O_2}{}^{2/3} \tag{12}$$

where n is the electron transfer number of ORR, F is the Faraday constant, V is the kinematic viscosity of 0.1 mol/L KOH electrolyte, C_{O_2} is the concentration of oxygen in aqueous solution, D_{O_2} is the diffusivity of oxygen. The related data about the calculation procedure are presented in Tables S1–S3 in the Supporting Information. The electron transfer number of ORR is determined to be 2.04 for β-FeC_2O_4·$2H_2O$ (Fig. 3b), indicating that O_2 is directly reduced to O_2^{2-} through a two-electron transfer pathway on the surface of β-FeC_2O_4·$2H_2O$. The coordinated H_2O molecules in β-FeC_2O_4·$2H_2O$ offer protons to react with O_2^{2-} to form H_2O_2 (Eq. 13) because ferrous ions of FeC_2O_4·$2H_2O$ can function as the Lewis acid site to scissor the O-H bond of the coordinated H_2O [43]. These results manifest that β-FeC_2O_4·$2H_2O$ possesses proper binding strength with O_2 for efficient H_2O_2 generation, thus avoiding the direct reduction of O_2 to H_2O. And then, the in-situ generated H_2O_2 can be efficiently activated to •OH by Fe(II) of β-FeC_2O_4·$2H_2O$, supplying continuous •OH stream for the subsequent oxidation of MC-LR.

$$O_2^{2-}+2H^+=H_2O_2 \tag{13}$$

3.4. The surface structure-dependent molecular oxygen activation property of β-FeC_2O_4·$2H_2O$

The morphology and structure of the β-FeC_2O_4·$2H_2O$ before and after reaction were characterized by SEM and TEM to obtain more details of molecular oxygen activation with β-FeC_2O_4·$2H_2O$. As shown in Fig. 4a, the fresh β-FeC_2O_4·$2H_2O$ has a cubic-like shape with a smooth surface. As for the used β-FeC_2O_4·$2H_2O$, its body surface is still smooth while the two ends are etched (Fig. 4b). Namely, the bottom and top surfaces are rough and hollowed-out after the reaction (Fig. 4b). Comparing Fig. 4c with 4d, the TEM images validate that oxygenation of β-FeC_2O_4·$2H_2O$ mainly happens at the bottom and top surfaces of β-FeC_2O_4·$2H_2O$, which indicates that the O_2 activation rests with the surface structure of β-FeC_2O_4·$2H_2O$.

In order to elucidate this surface-structure dependent O_2 activation process, high-resolution TEM analysis (HRTEM) was further employed to identify the exposed facet of the four lateral surfaces and the bottom and top surfaces of β-FeC_2O_4·$2H_2O$ according to the crystal lattice spacing. HRTEM image of the lateral surface exhibits clear lattice fringes with an interplanar lattice spacing of 0.261 nm and 0.189 nm, which correspond to the (0 2 2) facet and (0 2 6) facet, respectively (Fig. 4e). The corresponding selected area electron diffraction (SAED) pattern, indexed as the (4 0 0) zone, displays the single-crystalline characteristic of the β-FeC_2O_4·$2H_2O$ sample. The angle labeled in the SAED pattern is 27.4° (Fig. 4 g), which is identical to the theoretical value (Text S7 in SI) of the angle between the (0 2 2) and (0 2 6) facets. In addition, the HRTEM image of the bottom surface shows the lattice fringe spacing of 0.306 nm, which is assigned to the (4 0 0) facet of β-FeC_2O_4·$2H_2O$ (Fig. 4f). On the basis of the above results, the four lateral surfaces are (4 0 0) facets, while the (0 2 2) facet emerges on the top and bottom surfaces of β-FeC_2O_4·$2H_2O$ (Fig. 4h). The β-FeC_2O_4·$2H_2O$ (4 0 0) facet is of close-packed structures with high-density O atoms exposure (Fig. S9). The geometric structure of O_2 adsorbed on (4 0 0) facet was optimized by DFT calculation. As shown in Fig. 4i, the height of adsorption is 3.09 Å, indicating their weak interaction and thus ruling out the possibility of chemisorption. For comparison, β-FeC_2O_4·$2H_2O$ (0 2 2) facet possesses an open structure with Fe atom exposed (Fig. S10), which benefits the O_2 adsorption and subsequent molecular oxygen activation process. According to previous studies, the molecular oxygen activation pathways are strongly dependent on O_2 adsorption mode [44,45]. We then explored O_2 adsorption behavior on the β-FeC_2O_4·$2H_2O$ (0 2 2) facet and gained in-depth insight into how the surface properties controlled the molecular oxygen activation pathway. As shown in Fig. 4j and Table S4, O_2 can be adsorbed on the Fe site to form a side-on structure with an adsorption energy of − 1.74 eV. The O–O bond length is extended to 1.42 Å, which is close to that of O_2^{2-} (1.49 Å). Besides, O_2 can also interact with the Fe site by a perpendicular posture (end-on mode), the corresponding adsorption energy is − 1.62 eV and O–O bond length is prolonged to 1.27 Å, close to the bond lengths of $\bullet O_2^-$ (1.33 Å) (Fig. S11). According to the adsorption energies and the O-O bond length analysis, it can be inferred that O_2 prefers to combine with the Fe(II) site on β-FeC_2O_4·$2H_2O$ (0 2 2) facet through side-on mode, and the adsorbed O_2 is more likely to be reduced to O_2^{2-} species rather than $\bullet O_2^-$, which is consistent with above experimental results. Subsequently, we employed the deformation charge density difference to further elucidate the electron transfer pathway during O_2 activation processes on the β-FeC_2O_4·$2H_2O$ (0 2 2) facet. The image of charge density difference for O_2 adsorbed on the β-FeC_2O_4·$2H_2O$ (0 2 2) facet is shown in Fig. 4k. When the isovalue is set at 0.013 au, the electron cloud density of iron atoms in both out and inner layer oxide shell decreases, while the

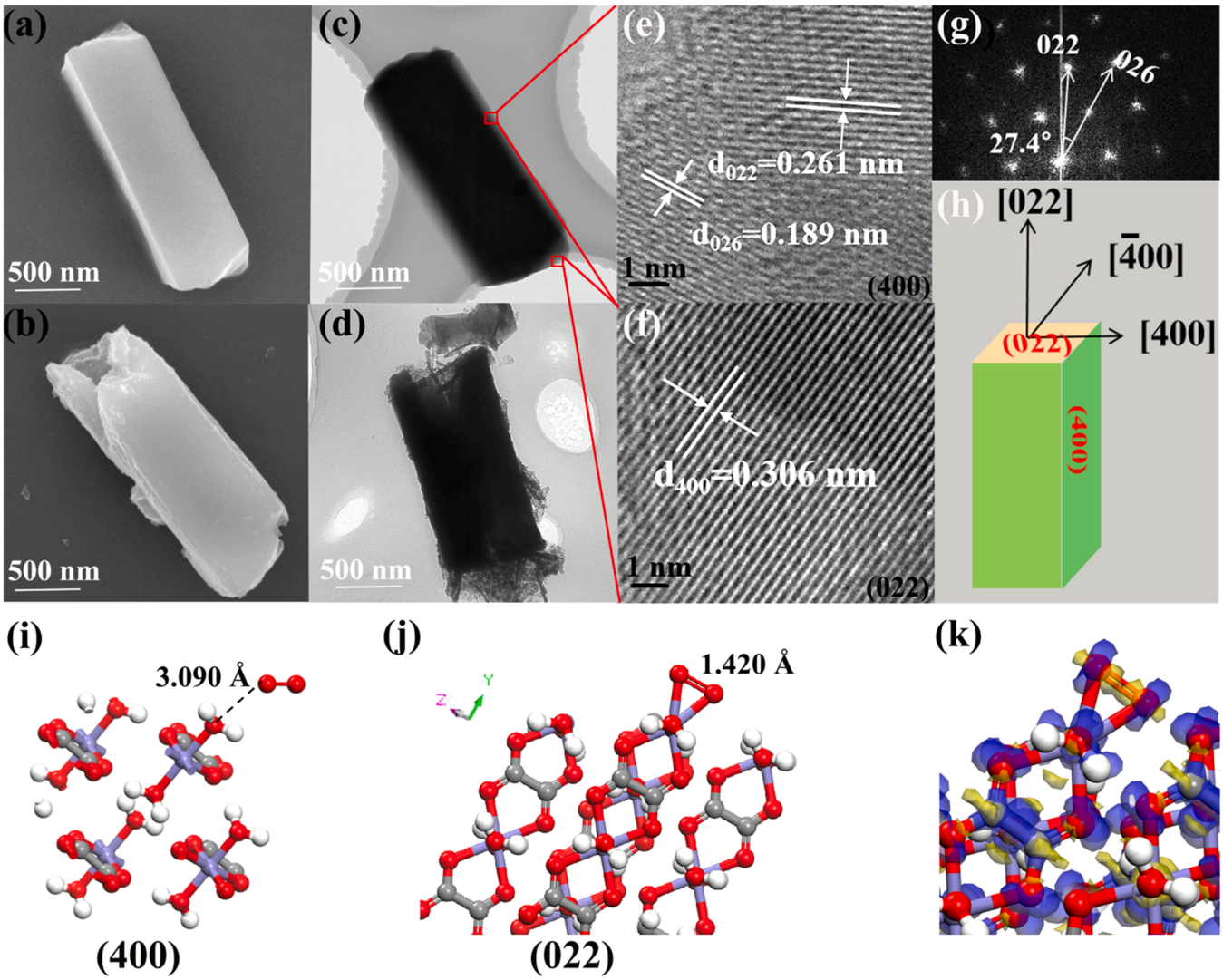

Fig. 4. The SEM image of β-$FeC_2O_4{\cdot}2H_2O$ (a) before and (b) after the reaction; The TEM image of β-$FeC_2O_4{\cdot}2H_2O$ (c) before and (d) after the reaction. (e-f) The HRTEM images of the β-$FeC_2O_4{\cdot}2H_2O$. (g) The selected-area electron diffraction (SAED) pattern of β-$FeC_2O_4{\cdot}2H_2O$. (h) Schematic illustration of the crystal orientation of β-$FeC_2O_4{\cdot}2H_2O$. (i) The geometry of O_2 adsorbed on (4 0 0) surface of β-$FeC_2O_4{\cdot}2H_2O$. (j) The geometry of O_2 adsorbed on (0 2 2) surface of β-$FeC_2O_4{\cdot}2H_2O$ in the side-on bound mode. (k) The charge density difference of the O_2 adsorbed on the (0 2 2) facet of β-$FeC_2O_4{\cdot}2H_2O$ in side-on bound mode. The blue and yellow isosurfaces represent charge accumulation and depletion in the space, respectively. The isovalue is 0.013 au.

electron cloud density of adsorbed O_2 increases. This result indicates that the direction of charge transfer is from β-$FeC_2O_4{\cdot}2H_2O$ to O_2 molecule. This electron transfer is originated from the back-donation of the d-orbital electron of Fe(II) to the π2p* orbitals of O_2. Such electron back-donation phenomenon is common in many iron-based catalysts, in which the adsorbed O_2 is activated to form reactive oxygen species [46].

3.5. Mechanism of ROS generation by β-$FeC_2O_4{\cdot}2H_2O$

According to above experimental and theoretical results, a plausible pathway of molecular oxygen activation with β-$FeC_2O_4{\cdot}2H_2O$ for •OH generation is illustrated below. Molecular oxygen is adsorbed onto the β-$FeC_2O_4{\cdot}2H_2O$ (0 2 2) surface through combining with the Fe(II) atom to form a side-on structure, then two electrons from Fe(II) sites transfer to the adsorbed O_2 and convert O_2 to O_2^{2-}. Afterward, the coordinated H_2O in the β-$FeC_2O_4{\cdot}2H_2O$ offers protons to react with O_2^{2-} to form H_2O_2 because ferrous ions of $FeC_2O_4{\cdot}2H_2O$ can function as the Lewis acid site to scissor the O–H bond of the coordinated H_2O. Finally, the in situ generated H_2O_2 can be efficiently activated to •OH by Fe(II) from β-$FeC_2O_4{\cdot}2H_2O$.

3.6. The durability of β-$FeC_2O_4{\cdot}2H_2O$ for aerobic degradation of MC-LR

The durability of β-$FeC_2O_4{\cdot}2H_2O$ is critical for its practical application in degradation of MC-LR. As depicted in Fig. 5a, β-$FeC_2O_4{\cdot}2H_2O$ maintains a high reactivity for aerobic degradation of MC-LR even in the fifth cycle, much better than previous reported iron-based materials, suggesting its outstanding durability. XRD patterns of the fresh and used β-$FeC_2O_4{\cdot}2H_2O$ in Fig. 5b demonstrate that the diffraction peaks of the β-$FeC_2O_4{\cdot}2H_2O$ become weaker as the reaction cycle increases, suggesting corrosion of β-$FeC_2O_4{\cdot}2H_2O$ takes place during the reaction. However, no new diffraction peak is observed in the XRD pattern of the used β-$FeC_2O_4{\cdot}2H_2O$, indicating the corrosion products are not deposited on the surface of β-$FeC_2O_4{\cdot}2H_2O$. The HR-XPS analysis was then applied to investigate the surface chemical characteristics of β-$FeC_2O_4{\cdot}2H_2O$ before and after reactions. The high-resolution spectrum of Fe 2p indicates co-existence of Fe(II) and Fe(III) species in the fresh-prepared β-$FeC_2O_4{\cdot}2H_2O$. Notably, the Fe(II)/Fe(III) molar ratio almost keeps unchanged regardless of the reaction cycles (Fig. 5c), indicating that no Fe(III) oxide/hydroxides is deposited on β-$FeC_2O_4{\cdot}2H_2O$ surface, which is consistent with that displayed by the SEM images. Nano spray

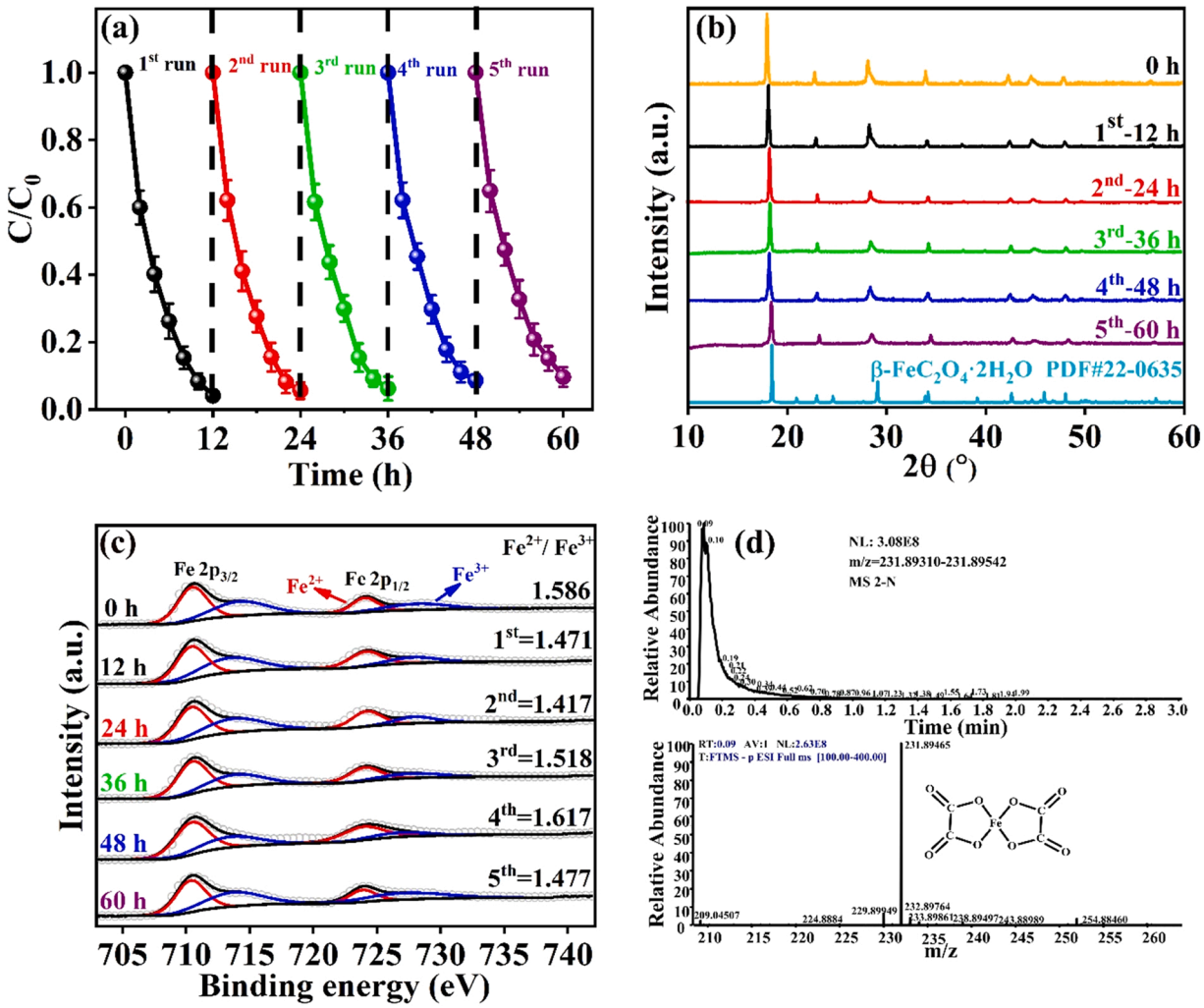

Fig. 5. (a) Reuse experiments of β-FeC_2O_4·$2H_2O$ for degradation of MC-LC in the presence of O_2. (b) XRD patterns of β-FeC_2O_4·$2H_2O$ before and after reactions; (c) High-resolution XPS profiles of Fe 2p of β-FeC_2O_4·$2H_2O$ before and after reactions. (d) The extracted ion chromatogram and mass spectra of [(Fe^{3+}-$(C_2O_4)_2$] (*m/z* 231.89465) detected in the β-FeC_2O_4·$2H_2O/O_2$ system.

LC-HRMS was subsequently employed to detect the oxygenation products of β-FeC_2O_4·$2H_2O$ in the aqueous solution. As shown in Fig. 5d, the $[Fe^{3+}$-$(C_2O_4^{2-})_2]^-$ complex (*m/z* 231.89465) with strong peak intensity (NL: 3.08 $\times 10^8$) is found in the negative ion mode. These results suggest that Fe(III) generated from oxidation of β-FeC_2O_4·$2H_2O$ would coordinate with oxalate anion to form soluble and stable $[Fe^{3+}$-$(C_2O_4^{2-})_2]^-$ complex (K_f ($[Fe^{3+}$-$(C_2O_4^{2-})_2]^- = 1.0 \times 10^{13}$), thus restraining Fe(III) oxide/hydroxide shell from depositing on β-FeC_2O_4·$2H_2O$ surface. This behavior addresses the surface passivation that usually occurs in the previous reported iron-based materials [47,48]. Therefore, β-FeC_2O_4·$2H_2O$ has remarkable durability in the degradation of MC-LR.

3.7. The possible degradation pathway and toxicity assessment

While O_2 activation by β-FeC_2O_4·$2H_2O$ has been proven to be an efficient strategy to degrade MC-LR in water, verifying the degradation intermediates and elucidating degradation pathway are needed to determine the detoxification efficiency. We employed LC-MS analysis to detect the transformation products during MC-LR degradation and 10 intermediates were identified (Figs. S12–S15). Based on these intermediates, a possible degradation pathway of MC-LR is proposed and demonstrated in Fig. 6. It is generally accepted that conjugated diene bonds are essential for the hepatotoxicity of MC-LR [49,50]. Fortunately, •OH is the primary oxidative species produced in β-FeC_2O_4·$2H_2O/O_2$ systems, and the diene bonds are considered to be the most vulnerable site to accept the attack from •OH [51]. The hydroxyl substitution occurs at C4 and C7 in the Adda group, producing Product A1 (*m/z* = 1011.5) and A2 (*m/z* = 1011.5). Further oxidative cleavage of bond C_7-C_8 of A1 and bond C_4-C_5 of A2 generate Product A3 (*m/z* = 835.4) and Product A4 (*m/z* = 795.4), respectively. Moreover, Product A3 can be degraded into Product A4 through destruction of the residual Adda group. Subsequently, Product A4 can be converted in Product A5 (*m/z* = 811.5) as the aldehyde group is oxidized to corresponding acid. Product A5 with intact cyclic structure then undergoes cleavage of peptide bonds via hydrolysis, producing Products B (B1 – B4, *m/z* = 829.4). Further splitting of the peptide bonds in Products B yields a number of small-molecule linear peptides (C1 *m/z* = 277.1, C2 *m/z* = 571.2, C3 *m/z* = 516.3, C4 *m/z* = 332.3, and C5 *m/z* = 243.1). In addition, the hepatotoxicities of MC-LR and its oxidation intermediates in the treated solutions were monitored by PP2A activity test. Associated results shown in Fig. S16 depict that the hepatotoxicity of solution drops with the decrease of MC-LR concentration, suggesting that MC-LR is readily degraded by •OH ($k = 2.3 \times 10^{10}$ M^{-1}•s^{-1}) in the β-FeC_2O_4·$2H_2O/O_2$ system and the final degradation products are not hepatotoxic [52]. This finding is in accordance with the degradation pathways of MC-LR in which the destruction of Adda side chain (the essential group for the hepatotoxicity of MC-LR) occurs initially.

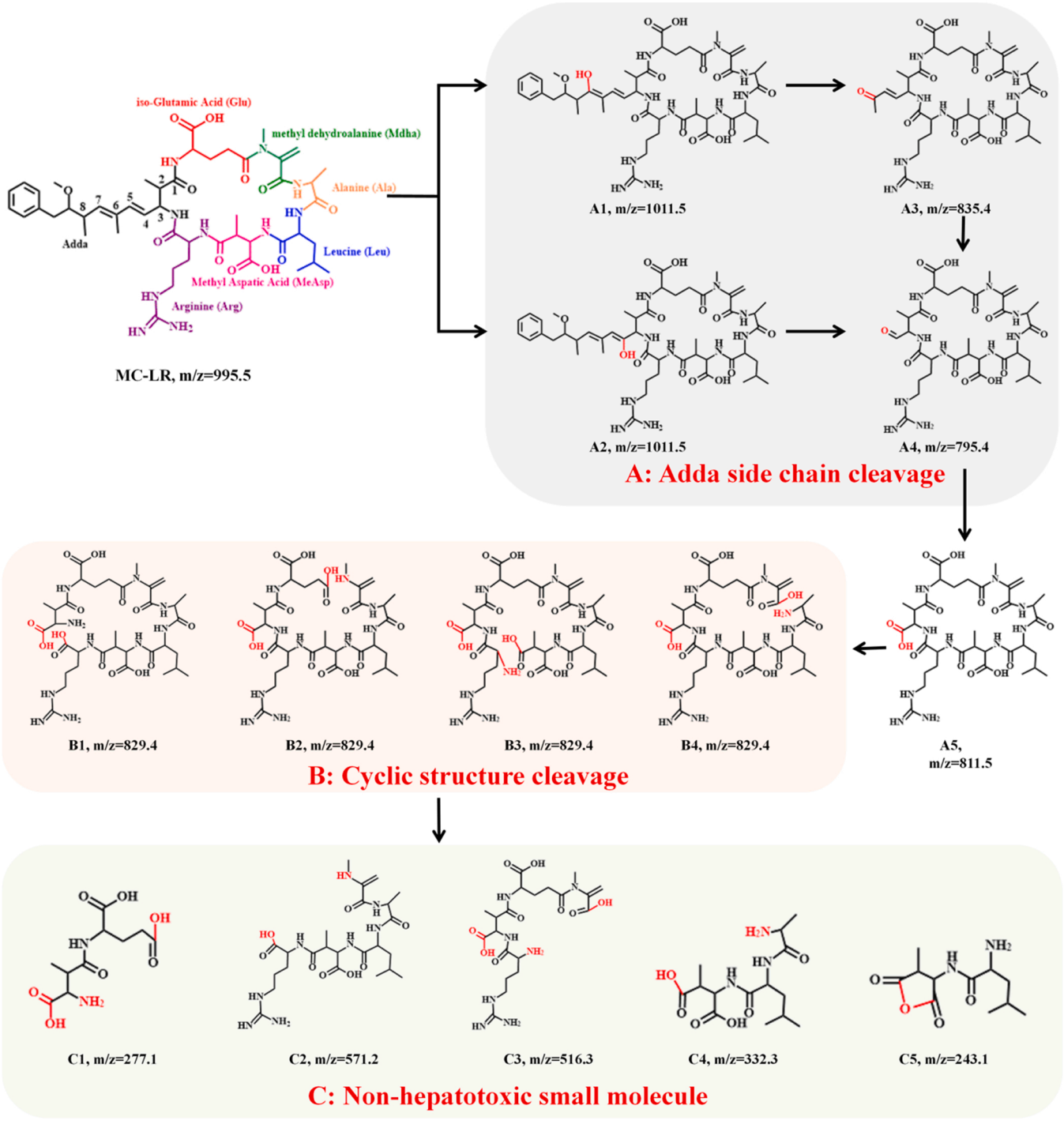

Fig. 6. Possible degradation pathway of MC-LR in the β-FeC_2O_4·2 H_2O/O_2 system.

3.8. *The impacts of environmental constituents and practical applicability*

In this study, the effects of the typical coexisting anions (such as Cl^-, SO_4^{2-}, and NO_3^-) on MC-LR degradation with β-FeC_2O_4·$2H_2O/O_2$ system were assessed as the coexisting anions could be adsorbed on the surface of β-FeC_2O_4·$2H_2O$ and consumed the surface-bound •OH. The results show that the coexisted inorganic ions studied have negligible effect on MC-LR degradation (Fig. S17). This is because the surface of β-FeC_2O_4·$2H_2O$ is negative charged (Fig. S18), which definitely curbs the adsorption of anions and subsequent consumption of surface-bound •OH. The impacts of initial pH values on MC-LR degradation by β-FeC_2O_4·$2H_2O/O_2$ were explored. As shown in Fig. S19, about 90.5%, 92.2%, 94.4%, 96.5%, 97.3% and 83.6% of MC-LR is removed in β-FeC_2O_4·$2H_2O/O_2$ system in 12 h when initial pH was 4.0, 5.0, 6.0, 7.0, 8.0 and 9.0, respectively. This result indicates that β-FeC_2O_4·$2H_2O$ has considerable activity for degrading MC-LR when pH ranges from 4.0 to 9.0. To examine the feasibility of β-FeC_2O_4·$2H_2O/O_2$ in the treatment of MC-LR contamination in realistic waters, the degradation of MC-LR was conducted in actual water sampled from Ganjiang River (the source of drinking water of Jiangxi Province, and detailed water quality parameters is provided in Table S5). As shown in Fig. S20, the degradation rate constant (0.2179 h^{-1}) in the Ganjiang River is close to that (0.2689 h^{-1}) in deionized waters. In addition, this β-FeC_2O_4·$2H_2O$ governing water treatment will not cause secondary contamination as $[Fe^{3+}$-$(C_2O_4^{2-})_2]^-$

complex, the oxygenation product of β-$FeC_2O_4{\cdot}2H_2O$, is environmental benign and widely existed in natural waters [53]. These results indicate that β-$FeC_2O_4{\cdot}2H_2O$ has a great potential in practical application in eliminating MC-LR in contaminated water or sources of water supply.

4. Conclusions

A novel approach concerning molecular oxygen activation for ROS generation was enabled by β-$FeC_2O_4{\cdot}2H_2O$, and introduced to eliminate MC-LR cyanotoxin in aqueous solution. Results from experimental and theoretical studies reveal that O_2 is reduced to H_2O_2 on the specific (0 2 2) facet of β-$FeC_2O_4{\cdot}2H_2O$ via a two-electron transfer pathway, followed by the generation of successive •OH stream from the activation of H_2O_2 by Fe(II). The electron utilization efficiency of β-$FeC_2O_4{\cdot}2H_2O$ toward •OH generation can approach 87.7%, which is much higher to those of reported iron-based materials. In addition, Fe^{3+} generated from β-$FeC_2O_4{\cdot}2H_2O$ oxygenation can coordinate with oxalate to form a soluble and stable $[Fe^{3+}\text{-}(C_2O_4^{2-})_2]^-$ complex in aqueous solution, which can avoid the surface passivation that is typically an issue encountered in iron-based materials. Transformation product analysis indicated that the •OH radicals attack the conjugated dienes (the essential group for the hepatotoxicity of MC-LR) in the Adda side chain as well as other sites in the Adda side chain and the cyclic structure. Moreover, the PP2A activity test revealed that hepatotoxicity of MC-LR is eliminated after the parent cyanotoxin is degraded, indicating the transformation products do not exhibit hepatotoxicity effects. In summary, this work opens a new avenue to activate molecular oxygen to produce •OH and delivers deep insight about the operation mechanism of β-$FeC_2O_4{\cdot}2H_2O$ on decomposing organic pollutants in aqueous solution.

CRediT authorship contribution statement

Qian Fu: Investigation, Writing – original draft, Formal analysis. **Yi Mu:** Investigation, Formal analysis, Conceptualization, Writing – original draft, Writing – review & editing, Project administration. **Lixia Yang:** Conceptualization, Methodology, Supervision, Writing – review & editing, Resources. **Yi Mei:** Investigation. **Meifeng Wu:** Investigation, Formal analysis. **Jian-Ping Zou:** Conceptualization, Supervision, Writing – review & editing, Resources. **Dionysios D. Dionysiou:** Supervision, Resources, Project administration. **Shenglian Luo:** Supervision, Methodology, Resources, Project administration.

Declaration of Competing Interest

The authors declare that they have no known competing financial interests or personal relationships that could have appeared to influence the work reported in this paper.

Data Availability

No data was used for the research described in the article.

Acknowledgments

This work was supported by National Science Foundation of China (51720105001, 21906076).

Associated Content.

Supporting Information.

Additional descriptions, Figures, and tables as mentioned in the text. This material is available free of charge via the Internet at http://www.sciencedirect.com.

Appendix A. Supporting information

Supplementary data associated with this article can be found in the online version at doi:10.1016/j.apcatb.2022.121970.

References

[1] D. Drobac, N. Tokodi, J. Simeunović, V. Baltić, D. Stanić, Z. Svirčev, Human exposure to cyanotoxins and their effects on health, Arch. Ind. Hyg. Toxicol. 64 (2013) 305–316, https://doi.org/10.2478/10004-1254-64-2013-2320.
[2] M. Jang, D.E. Berthold, Z. Yu, C. Silva-Sanchez, H.D. Laughinghouse, N. D. Denslow, S. Han, Atmospheric progression of microcystin-LR from cyanobacterial aerosols, Environ. Sci. Technol. Lett. 7 (2020) 740–745, https://doi.org/10.1021/acs.estlett.0c00464.
[3] H. Li, M. Barber, J. Lu, R. Goel, Microbial community successions and their dynamic functions during harmful cyanobacterial blooms in a freshwater lake, Water Res. 185 (2020), 116292, https://doi.org/10.1016/j.watres.2020.116292.
[4] M.G. Antoniou, A.A. De La Cruz, D.D. Dionysiou, Degradation of microcystin-LR using sulfate radicals generated through photolysis, thermolysis and e^- transfer mechanisms, Appl. Catal. B: Environ. 96 (2010) 290–298, https://doi.org/10.1016/j.apcatb.2010.02.013.
[5] World Health Organization, Guidelines for drinking-water quality (4th ed.), incorporating the first addendum, Geneva (2017). ⟨https://www.who.int/publications/i/item/9789241549950⟩.
[6] E.R. Bandala, D. Martínez, E. Martínez, D.D. Dionysiou, Degradation of microcystin-LR toxin by Fenton and Photo-Fenton processes, Toxicon 43 (2004) 829–832, https://doi.org/10.1016/j.toxicon.2004.03.013.
[7] W. Liao, M. Murugananthan, Y. Zhang, Electrochemical degradation and mechanistic analysis of microcystin-LR at boron-doped diamond electrode, Chem. Eng. J. 243 (2014) 117–126, https://doi.org/10.1016/j.cej.2013.12.091.
[8] X. Zhang, J. He, Y. Lei, Z. Qiu, S. Cheng, X. Yang, Combining solar irradiation with chlorination enhances the photochemical decomposition of microcystin-LR, Water Res. 159 (2019) 324–332, https://doi.org/10.1016/j.watres.2019.05.030.
[9] J.J. Chen, Y.Y. Zhang, Quasi-3-D gadolinium iodate constructed from infinite polyiodate: structure, green-emission and UV light-driven degradation on organic dye, Chin. J. Struct. Chem. 39 (2020) 1323–1330, https://doi.org/10.14102/j.cnki.0254-5861.2011-2581.
[10] M. Pelaez, A. Armah, K. O'Shea, P. Falaras, D.D. Dionysiou, Effects of water parameters on the degradation of microcystin-LR under visible light-activated TiO_2 photocatalyst, Water Res. 45 (2011) 3787–3796, https://doi.org/10.1016/j.watres.2011.04.036.
[11] Y.W. Huang, J.Y. Mao, Q.R. Qian, H. Xue, Y.R. Liu, Study on the different photocatalytic performances for tetracycline hydrochloride degradation of p-block metal composite oxides Sr1.36Sb2O6 and Sr2Sb2O7, Chin. J. Struct. Chem. 40 (2021) 394–402, https://doi.org/10.14102/j.cnki.0254-5861.2011-3105.
[12] M. Metz, E.I. Solomon, Dioxygen binding to deoxyhemocyanin: electronic structure and mechanism of the spin-forbidden two-electron reduction of O_2, J. Am. Chem. Soc. 123 (2001) 4938–4950, https://doi.org/10.1021/ja004166b.
[13] L. Pi, J. Cai, L. Xiong, J. Cui, H. Hua, D. Tang, X. Mao, Generation of H_2O_2 by on-site activation of molecular dioxygen for environmental remediation applications: a review, Chem. Eng. J. 389 (2020), 123420, https://doi.org/10.1016/j.cej.2019.123420.
[14] F. Fu, D.D. Dionysiou, H. Liu, The use of zero-valent iron for groundwater remediation and wastewater treatment: a review, J. Hazard. Mater. 267 (2014) 194–205, https://doi.org/10.1016/j.jhazmat.2013.12.062.
[15] S. Hu, B. Liu, D. Wang, L. Wu, K. Xiao, S. Liang, H. Hou, J. Yang, In situ generation of zero valent iron for enhanced hydroxyl radical oxidation in an electrooxidation system for sewage sludge dewatering, Water Res. 145 (2018) 162–171, https://doi.org/10.1016/j.watres.2018.08.027.
[16] S.H. Joo, A.J. Feitz, D.L. Sedlak, T.D. Waite, Quantification of the oxidizing capacity of nanoparticulate zero-valent iron, Environ. Sci. Technol. 39 (2005) 1263–1268, https://doi.org/10.1021/es048983d.
[17] D. Cheng, S. Yuan, P. Liao, P. Zhang, Oxidizing impact induced by mackinawite (FeS) nanoparticles at oxic conditions due to production of hydroxyl radicals, Environ. Sci. Technol. 50 (2016) 11646–11653, https://doi.org/10.1021/acs.est.6b02833.
[18] D. Cheng, W. Liao, S. Yuan, Effect of in situ generated iron oxyhydroxide coatings on FeS oxygenation and resultant hydroxyl radical production for contaminant degradation, Chem. Eng. J. 394 (2020), 124961, https://doi.org/10.1016/j.cej.2020.124961.
[19] M.Q. Cai, Y.Z. Zhu, Z.S. Wei, J.Q. Hu, S.D. Pan, R.Y. Xiao, C.Y. Dong, M.C. Jin, Rapid decolorization of dye Orange G by microwave enhanced Fenton-like reaction with delafossite-type $CuFeO_2$, Sci. Total Environ. 580 (2017) 966–973, https://doi.org/10.1016/j.scitotenv.2016.12.047.
[20] Y. Sun, Z. Yang, P. Tian, Y. Sheng, J. Xu, Y.F. Han, Oxidative degradation of nitrobenzene by a Fenton-like reaction with Fe-Cu bimetallic catalysts, Appl. Catal. B: Environ. 244 (2019) 1–10, https://doi.org/10.1016/j.apcatb.2018.11.009.
[21] C.R. Keenan, D.L. Sedlak, Factors Affecting the yield of oxidants from the reaction of nanoparticulate zero-valent iron and oxygen, Environ. Sci. Technol. 42 (2008) 1262–1267, https://doi.org/10.1021/es7025664.
[22] Y. Pan, M. Zhou, Q. Wang, J. Cai, Y. Tian, Y. Zhang, EDTA, oxalate, and phosphate ions enhanced reactive oxygen species generation and sulfamethazine removal by zero-valent iron, J. Hazard. Mater. 391 (2020), 122210, https://doi.org/10.1016/j.jhazmat.2020.122210.
[23] R. Peng, J. Shao, Y. Xie, A. Chen, L. Peng, Q. Zeng, S. Luo, Oxalate-enhanced reactivity of nanoscale zero-valent iron under different conditions of O_2, N_2 or without aeration, Chem. Eng. J. 330 (2017) 398–406, https://doi.org/10.1016/j.cej.2017.07.154.
[24] C. Lee, C.R. Keenan, D.L. Sedlak, Polyoxometalate-enhanced oxidation of organic compounds by nanoparticulate zero-valent iron and ferrous ion in the presence of

oxygen, Environ. Sci. Technol. 42 (2008) 4921–4926, https://doi.org/10.1016/j.watres.2015.06.016.
[25] L. Wang, F. Wang, P. Li, L. Zhang, Ferrous-tetrapolyphosphate complex induced dioxygen activation for toxic organic pollutants degradation, Sep. Purif. Technol. 120 (2013) 148–155, https://doi.org/10.1016/j.seppur.2013.10.002.
[26] Y. Xu, L. Zeng, L. Li, Y.S. Chang, J. Gong, Enhanced oxidative activity of zero-valent iron by citric acid complexation, Chem. Eng. J. 373 (2019) 891–901, https://doi.org/10.1016/j.cej.2019.05.093.
[27] Y.X. Qin, G.Y. Li, L.Z. Zhang, T.C. An, Protocatechuic acid promoted catalytic degradation of rhodamine B with Fe@Fe_2O_3 core-shell nanowires by molecular oxygen activation mechanism, Catal. Today 335 (2019) 144–150, https://doi.org/10.1016/j.cattod.2018.10.058.
[28] C.E. Noradoun, I.F. Cheng, EDTA degradation induced by oxygen activation in a zerovalent iron/air/water system, Environ. Sci. Technol. 39 (2005) 7158–7163, https://doi.org/10.1021/es050137v.
[29] A. Kulkarni, S. Siahrostami, A. Patel, J.K. Nørskov, Understanding catalytic activity trends in the oxygen reduction reaction, Chem. Rev. 118 (2018) 2302–2312, https://doi.org/10.1021/acs.chemrev.7b00488.
[30] Z. Lu, G. Chen, S. Siahrostami, Z. Chen, K. Liu, J. Xie, L. Liao, T. Wu, D. Lin, Y. Liu, T.F. Jaramillo, J.K. Nørskov, Y. Cui, High-efficiency oxygen reduction to hydrogen peroxide catalysed by oxidized carbon materials, Nat. Catal. 1 (2018) 156–162, https://doi.org/10.1038/s41929-017-0017-x.
[31] J. Guo, X. Yan, Q. Liu, Q. Li, X. Xu, L. Kang, Z. Cao, G. Chai, J. Chen, Y. Wang, J. Yao, The synthesis and synergistic catalysis of iron phthalocyanine and its graphene-based axial complex for enhanced oxygen reduction, Nano Energy 46 (2018) 347–355, https://doi.org/10.1016/j.nanoen.2018.02.026.
[32] X. Shen, F. Xiao, H. Zhao, Y. Chen, C. Fang, R. Xiao, W. Chu, G. Zhao, In situ-formed PdFe nanoalloy and carbon defects in cathode for synergic reduction-oxidation of chlorinated pollutants in electro-Fenton process, Environ. Sci. Technol. 54 (2020) 4564–4572, https://doi.org/10.1021/acs.est.9b05896.
[33] X. Fan, L. Zhang, M. Li, M. Wang, X. Zhou, R. Cheng, Y. Zhou, J. Shi, α-Ferrous oxalate dihydrate: a simple coordination polymer featuring photocatalytic and photo-initiated Fenton oxidations, Sci. China Mater. 59 (2016) 574–580, https://doi.org/10.1007/s40843-016-5064-y.
[34] L. Hu, P. Wang, S. Xiong, S. Chen, X. Yin, L. Wang, H. Wang, The attractive efficiency contributed by the in-situ reactivation of ferrous oxalate in heterogeneous Fenton process, Appl. Surf. Sci. 467 (2019) 185–192, https://doi.org/10.1016/j.apsusc.2018.10.151.
[35] N. Chen, Y. Zhao, M.Q. Li, X.B. Wang, X. Peng, H.W. Sun, L.Z. Zhang, $FeC_2O_4{\cdot}2H_2O$ enables sustainable conversion of hydrogen peroxide to hydroxyl radical for promoted mineralization and detoxification of sulfadimidine, J. Hazard. Mater. 436 (2022), 129049, https://doi.org/10.1016/j.jhazmat.2022.129049.
[36] R. James, A. Gregg, A. Dindal, J. McKernan, Environmental Technology Verification Report Microcystest kit, (2011). ⟨https://nepis.epa.gov/Exe/ZyPDF.cgi?Dockey=P100ELW3.txt⟩.
[37] Y. Mu, Z. Ai, L. Zhang, Phosphate shifted oxygen reduction pathway on Fe@Fe_2O_3 core-shell nanowires for enhanced reactive oxygen species generation and aerobic 4-chlorophenol degradation, Environ. Sci. Technol. 51 (2017) 8101–8109, https://doi.org/10.1021/acs.est.7b01896.
[38] J. He, C.J. Miller, R. Collins, D. Wang, T.D. Waite, Production of a surface-localized oxidant during oxygenation of mackinawite (FeS), Environ. Sci. Technol. 54 (2020) 1167–1176, https://doi.org/10.1021/acs.est.9b03975.
[39] H. Sun, J. Wang, Y. Jiang, W. Shen, F. Jia, S. Wang, X. Liao, L. Zhang, Rapid aerobic inactivation and facile removal of *Escherichia coli* with amorphous zero-valent iron microspheres: indispensable roles of reactive oxygen species and iron corrosion products, Environ. Sci. Technol. 53 (2019) 3707–3717, https://doi.org/10.1021/acs.est.8b06499.
[40] H. Che, X. Gao, J. Chen, J. Hou, Y. Ao, P. Wang, Iodide-induced fragmentation of polymerized hydrophilic carbon nitride for high performance quasi-homogeneous photocatalytic H_2O_2 production, Angew. Chem. Int. Ed. 60 (2021) 25546–25550, https://doi.org/10.1002/anie.202111769.
[41] Y. Wu, J. Chen, H. Che, X. Gao, Y. Ao, P. Wang, Boosting $2e^-$ oxygen reduction reaction in garland carbon nitride with carbon defects for high-efficient photocatalysis-self-Fenton degradation of 2,4-dichlorophenol, Appl. Catal. B: Environ. 307 (2022), 121185, https://doi.org/10.1016/j.apcatb.2022.121185.
[42] H. Sheng, H. Ji, W. Ma, C. Chen, J. Zhao, Direct four-electron reduction of O_2 to H_2O on TiO_2 surfaces by pendant proton relay, Angew. Chem. Int. Ed. 52 (2013) 9686–9690, https://doi.org/10.1002/ange.201304481.
[43] T. Yamada, M. Sadakiyo, H. Kitagawa, High proton conductivity of one-dimensional ferrous oxalate dihydrate, J. Am. Chem. Soc. 131 (2009) 3144–3145, https://doi.org/10.1021/ja808681m.
[44] H. Li, Z.H. Ai, L.Z. Zhang, Surface structure-dependent photocatalytic O_2 activation for pollutant removal with bismuth oxyhalides, Chem. Commun. 56 (2020) 15282–15296, https://doi.org/10.1039/d0cc05449f.
[45] K. Zhao, L.Z. Zhang, J.J. Wang, Q.X. Li, W.W. He, J.J. Yin, Surface structure-dependent molecular oxygen activation of BiOCl single-crystalline nanosheets, J. Am. Chem. Soc. 135 (2013) 15750–15753, https://doi.org/10.1021/ja4092903.
[46] S. Han, H. Kim, J. Kim, Y. Jung, Modulating the magnetic behavior of Fe(II)-MOF-74 by the high electron affinity of the guest molecule, Phys. Chem. Chem. Phys. 17 (2015) 16977–16982, https://doi.org/10.1039/c5cp01441g.
[47] B. Flury, J. Frommer, U. Eggenberger, U. Mäder, M. Nachtegaal, R. Kretzschmar, Assessment of long-term performance and chromate reduction mechanisms in a field scale permeable reactive barrier, Environ. Sci. Technol. 43 (2009) 6786–6792, https://doi.org/10.1021/es803526g.
[48] X. Guan, Y. Sun, H. Qin, J. Li, I.M. Lo, D. He, H. Dong, The limitations of applying zero-valent iron technology in contaminants sequestration and the corresponding countermeasures: the development in zero-valent iron technology in the last two decades (1994-2014), Water Res. 75 (2015) 224–248, https://doi.org/10.1016/j.watres.2015.02.034.
[49] R.M. Dawson, the toxicology of microcystins, Toxicon 36 (1998) 953–962, https://doi.org/10.1016/s0041-0101(97)00102-5.
[50] E.M. Rodriguez, J.L. Acero, L. Spoof, J. Meriluoto, Oxidation of MC-LR and -RR with chlorine and potassium permanganate: toxicity of the reaction products, Water Res. 42 (2008) 1744–1752, https://doi.org/10.1016/j.watres.2007.10.039.
[51] M. Nawaz, M. Moztahida, J. Kim, A. Shahzad, J. Jang, W. Miran, D.S. Lee, Photodegradation of microcystin-LR using graphene-TiO_2/sodium alginate aerogels, Carbohydr. Polym. 199 (2018) 109–118, https://doi.org/10.1016/j.carbpol.2018.07.007.
[52] W. Song, T. Xu, W.J. Cooper, D.D. Dionysiou, A.A. De La Cruz, K.E. O'Shea, Radiolysis studies on the destruction of microcystin-LR in aqueous solution by hydroxyl radicals, Environ. Sci. Technol. 43 (2009) 1487–1492, https://doi.org/10.1021/es802282n.
[53] L.H. Kong, M.C. He, Mechanisms of Sb(III) photooxidation by the excitation of organic Fe(III) complexes, Environ. Sci. Technol. 50 (2016) 6974–6982, https://doi.org/10.1021/acs.est.6b00857.